Modeling of lower mantle seismic anisotropy beneath subduction zones

S. E. J. Nippress,[1] N. J. Kusznir,[1] and J.-M. Kendall[2]

Received 8 June 2004; revised 13 August 2004; accepted 15 September 2004; published 14 October 2004.

[1] Recent observations of up to 6 secs of shear-wave splitting in deep focus earthquakes from the Tonga-Kermadec subduction zone provide insights into mantle dynamics near the 660 km discontinuity. Modeling of subduction body force stresses predicts large deviatoric stress (~40 MPa) in the topmost lower mantle below a viscosity increase at the 660 km discontinuity. Finite strain calculations produce significant amounts of natural strains (~7) in the lower mantle, and coherently aligned strain ellipses. For a viscosity model with a viscosity increase at 660 km, 5–10 secs of shear-wave splitting is predicted, compared to only 0–5 secs for uniform mantle viscosity. For a viscosity increase model, we predict that shear-wave splitting reduces from 7–10 secs to 4–6 secs when deformation above 410 km is ignored, and further reduces to 2–3 secs when deformation above 660 km is zeroed. Various conversions from finite strain to anisotropy have been explored. Predicted shear-wave splitting magnitudes are comparable to those observed from the Tonga-Kermadec subduction zone. *INDEX TERMS:* 1213 Geodesy and Gravity: Earth's interior—dynamics (8115, 8120); 7207 Seismology: Core and mantle; 8168 Tectonophysics: Stresses—general. **Citation:** Nippress, S. E. J., N. J. Kusznir, and J.-M. Kendall (2004), Modeling of lower mantle seismic anisotropy beneath subduction zones, *Geophys. Res. Lett.*, *31*, L19612, doi:10.1029/2004GL020701.

1. Introduction

[2] There is abundant evidence for seismic anisotropy in the upper mantle [e.g., *Silver*, 1996; *Fischer and Wiens*, 1996] extending to the base of the olivine stability field at 410 km. The mantle between 410 km and the D″ was thought to be isotropic, until recent observations suggested weak anisotropy [e.g., *Vinnik et al.*, 1998; *Trampert and van Heijst*, 2002]. *Wookey et al.* [2002] analysed deep focus events (>300 km depth) from the Tonga-Kermadec subduction zone to Australian stations and observed shear-wave splitting generally between 3 and 6 secs. They showed that the shear-wave splitting observations are generated by near-source anisotropy located in the topmost lower mantle.

[3] The cause of the anisotropy in the topmost lower mantle is unknown, however large body force stresses created by a viscosity increase at the 660 km discontinuity impeding a sinking subducting slab [*Kusznir*, 2000] provide a potential mechanism for the alignment of crystals or inclusions, which generates seismic anisotropy. We investigate the possible cause of anisotropy in the topmost lower mantle observed by *Wookey et al.* [2002] using numerical geodynamic modelling and seismic ray-tracing.

2. Subduction Body Force Stresses and Mantle Viscosity Structure

[4] We use the 2D finite element method (FE) to predict subduction zone stresses arising from incompressible fluid flow driven by the body forces arising from the negative buoyancy of the subducting slab. We do not aim to model the development of subduction, only the flow and stress field at the point when subducted slab reaches the 660 km phase transition. The FE model extends from the surface to the base of the mantle with zero vertical velocity at model top and bottom. The FE model is driven dynamically by the excess density (~50 kgm^{-3}) of the subducting slab within the upper mantle, rather than by using plate-velocity boundary conditions. The density field of the subducting slab extends to 660 km, dips at 60° and has constant geometry with time. Starting with an initial mantle geotherm, subduction temperatures are modelled by a coupled diffusion-advection solution using advection velocities from the FE fluid flow solution. Modeled temperatures compare well to other studies [e.g., *Sleep*, 1973] and the predicted excess density of the subducted slab is consistent with that used to drive the FE flow model. Both flow and stresses resulting from subduction are dependant on the viscosity structure of the upper and lower mantle. Models of mantle viscosity structure show a broad range of viscosity increase with depth from the asthenosphere to the lower mantle and across the 410 km and 660 km phase transitions [e.g., *King*, 1995; *Kaufmann and Lambeck*, 2000; *Steinberger and Holme*, 2002]. We explore the effect that mantle viscosity structure has on subduction body force stresses and the generation of seismic anisotropy. The slab is treated as a viscous fluid with a viscosity of 10^{21} Pas.

[5] Deviatoric stresses calculated for the subduction model, as the subducted slab reaches the 660 km phase transition, are shown in Figures 1a and 1b for the *Steinberger* [2000] viscosity-depth profile (model A) based on postglacial rebound and geoid data, and for a uniform mantle viscosity (model B). The viscosity models used in sensitivity tests are shown in Figure 2. The Steinberger viscosity-depth model (model A) generates deviatoric stresses of the order of 40 MPa over a large region in the topmost lower mantle with lateral wavelength ~800 km and depth extent ~900 km. In contrast, the uniform mantle viscosity profile (model B) only generates significant magnitudes of deviatoric stress in the lithosphere and subducting slab. It is these topmost lower mantle stresses of model A, which may induce

[1]Department of Earth and Ocean Sciences, University of Liverpool, Liverpool, UK.
[2]School of Earth Sciences, University of Leeds, Leeds, UK.

0094-8276/04/2004GL020701$05.00

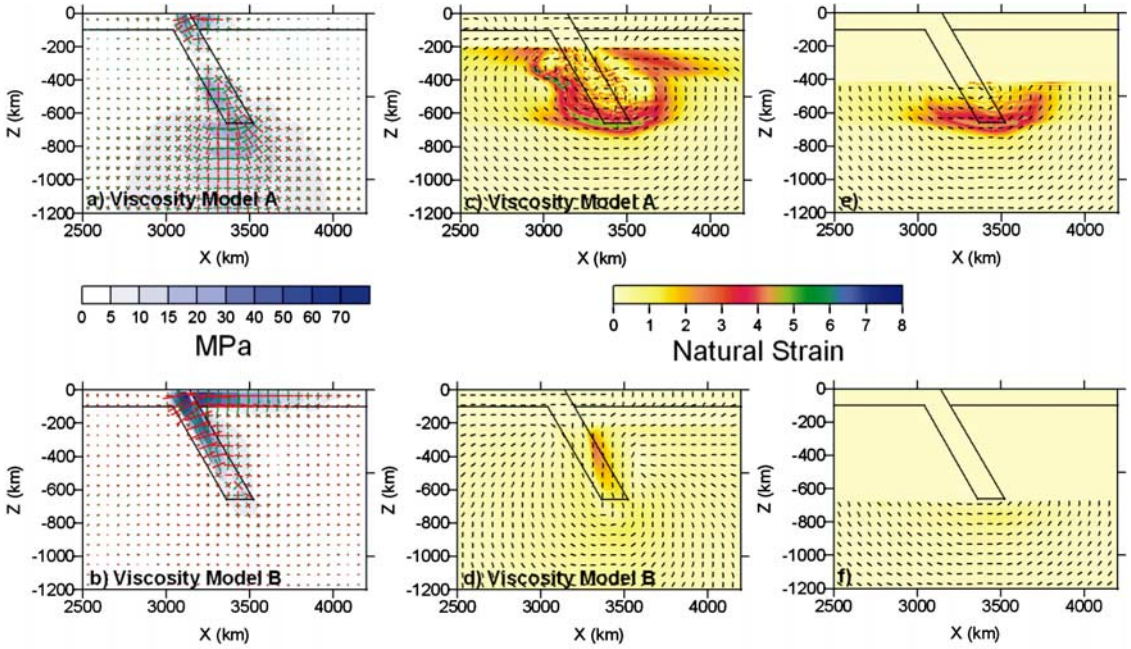

Figure 1. (a–b) Deviatoric stress magnitudes calculated using viscosity models A and B. Red = compressional and green = tensile. Shading intensity indicates the magnitude of maximum shear stress. The position of the subducting slab is shown. (c–d) Natural strain and orientation of the finite strain ellipse for viscosity model A and B. Natural strain magnitude shown by shading and the orientation shown by the black eigenvectors. (e–f) Stresses for deformation memory zeroed above 410 km and 660 km both for viscosity model A.

mineral alignment and thus generate the observed seismic anisotropy.

3. Prediction of Seismic Anisotropy From Finite Strain

[6] Observational evidence and theoretical predictions [*Ben Ismail and Mainprice*, 1998; *Wenk et al.*, 1991] show that the fast shear-wave orientation aligns with the maximum extensional strain axes in olivine. *Blackman and Kendall* [2002] suggest that simple flow fields produce finite strain ellipse orientations that match fast seismic directions determined for texture models. Consequently, we use the calculation of finite strain as a first order approximation to calculating seismic anisotropy surrounding a subducting slab. Our subduction models are two-dimensional and therefore we assume that there is no deformation in the third dimension.

[7] We use the formulation of *Malvern* [1969] and *McKenzie* [1979] to calculate the finite strain accumulated by a mantle parcel as it travels along a streamline. In a Eulerian description the evolution of **F** (deformation tensor) is determined using

$$\frac{\partial}{\partial t}(\mathbf{F}) = \mathbf{LF} - \mathbf{v}.(\nabla \mathbf{F}), \qquad (1)$$

where **L** is the velocity gradient tensor calculated from the steady state FE fluid flow. **F** is calculated by integration for a time duration corresponding to that required for slab material to reach the 660 km phase transition. The initial condition of **F** is the identity matrix corresponding to zero deformation. From **F** we calculate the Green deformation tensor, **B**, and the left hand stretch tensor **V**. The eigenvalues and eigenvectors of $\mathbf{V}^2$ describe the exact shape of the finite strain ellipse. Our approach is similar to that of *Hall et al.* [2000], however Hall et al. calculate finite strain using $\mathbf{B}^{-1}$. They perform an eigenvalue decomposition on $\mathbf{B}^{-1}$ and define a stretching ratio from the deformed to undeformed state in the direction of the i-th eigenvector of $\mathbf{B}^{-1}$. Both approaches yield the same result, but numerically $\mathbf{V}^2$ is faster to calculate and is used in this study. The amount of strain is displayed by plotting the natural strain ($\zeta = \mathrm{LOG}_{10}(\lambda_1/\lambda_2)$) and the orientation of the major axes.

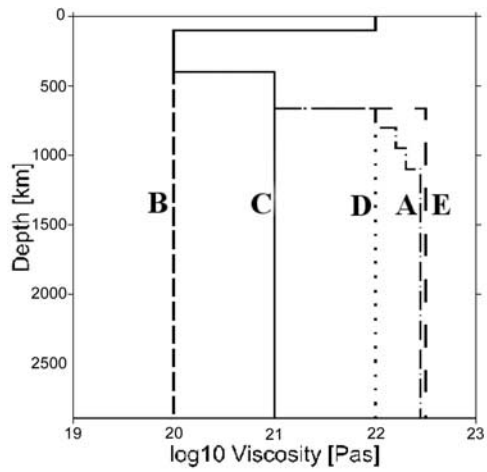

Figure 2. Viscosity models A–E used to calculate subduction body force stresses and finite deformation.

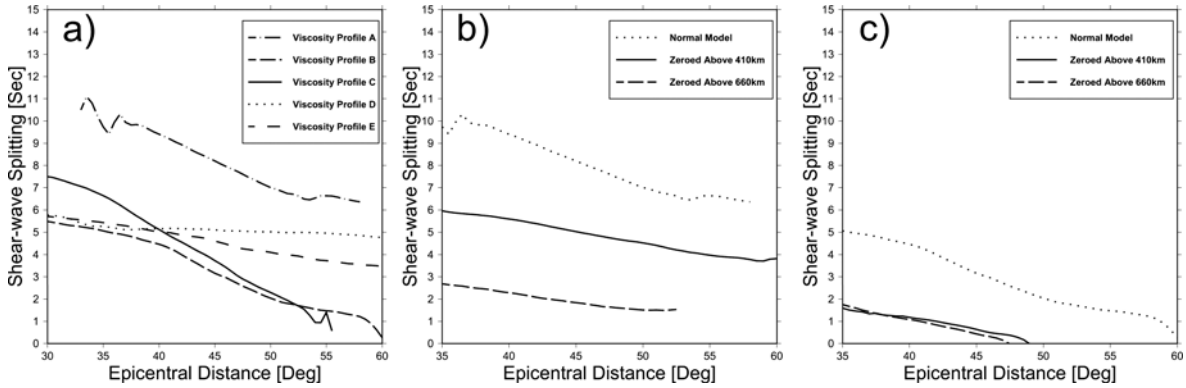

Figure 3. (a) Shear-wave splitting from ray-tracing through anisotropy models generated by viscosity models A–E. Shear-wave splitting from anisotropy showing the effect of zeroing deformation at 410 km and 660 km for (b) viscosity model A and (c) viscosity model B.

[8] The resulting natural strain and major axes orientation for viscosity models A and B are compared in Figures 1c and 1d and show a significant difference in the strains generated by the two viscosity profiles. Viscosity model A produces a region of large natural strain (~7) in the topmost lower mantle in a region comparable to that with large deviatoric stresses. The orientations of the major strain axes also show a coherent alignment, which is required to generate seismic anisotropy. In comparison, only a minor amount of natural strain (~2) is generated in the top of the lower mantle by model B. The orientation patterns of the major axes of strain we produce in the upper mantle are complex but are comparable to other studies [e.g., *Fischer et al.*, 2000].

[9] We conduct numerical experiments using viscosity model A to explore the consequences of inherited deformation for minerals that have undergone phase transitions at 410 km (olivine to spinel) and 660 km (spinel to perovskite) during subduction. Figure 1e shows that the effect of setting to zero the inherited deformation from above 410 km produces only a small reduction in the magnitude of natural strain in the region around 660 km (max ~5). The effect of zeroing deformation above 660 km is much more significant (Figure 1f), resulting in a reduction of natural strain from approximately 7 to 2 for the region below 660 km.

[10] The conversion from finite strain to seismic anisotropy for perovskite is not well understood and consequently we have tested three conversions schemes. Conversion (i) is based on rock deformation studies on olivine by *Ribe* [1992], in which anisotropy increases rapidly at small strains before saturating at a finite strain of 1.5, and is considered because no alternative conversions are available for lower mantle minerals. We also consider conversions which use: (ii) a linear scaling of finite strain to anisotropy which saturates more slowly than the Ribe curve at a finite strain of 3.5; and (iii) an exponential scaling that saturates more quickly than the Ribe curve at a finite strain of 0.5. The magnitude of anisotropy due to LPO of a polycrystalline aggregate is about $^1/_3 - ^1/_2$ of that of a perfectly orientated single crystal [*Karato*, 1998] reducing the seismic anisotropy ~26% for a perovskite single crystal [*Mainprice et al.*, 2000] to a maximum magnitude S-wave anisotropy of 13% for mantle material. An important limitation of all of these conversions is that they do not consider dynamic recrystallization, which is thought to partially randomize mineral orientation [*Ribe*, 1992]. However, given our limited knowledge of such processes in the lower mantle, we neglect this effect.

4. Prediction of Shear-Wave Splitting for the Tonga-Kermadec Subduction Zone

[11] In order to calculate shear-wave splitting we trace seismic rays through the finite strain models in a 2D multi-layered, inhomogeneous, anisotropic media, which requires mantle velocities and densities. The density of the mantle is calculated using PREM [*Dziewonski and Anderson*, 1981] with the addition of the slab density as used in the FE calculation. Mantle velocities are temperature dependant and the values given by PREM are modified to include the effects of subduction. The formulation of *Sleep* [1973] is used to compute mantle velocities from temperature. The ray tracing requires an anisotropic elastic model to be constructed which we calculate using the Thomsen parameters [*Thomsen*, 1986], mantle densities, P- and S-wave velocities. The Thomsen parameters are assumed to be the same (i.e., elliptical anisotropy) and by definition describe a transversely isotropic medium (hexagonal symmetry). The symmetry axis is then aligned with the major axis of the finite strain ellipse.

[12] We place a seismic source at the base of the subducting slab (660 km) and use an anisotropic ray tracer to trace rays to a depth of 1200 km. Beneath 1200 km the models are assumed to be isotropic; and we then ray-trace through the PREM velocity model to teleseismic distances using the TauP toolkit [*Crotwell et al.*, 1999]. We plot total travel-time against epicentral distance and calculate shear-wave splitting.

[13] Figure 3a, shows predicted shear-wave splitting arising from subduction body force stresses for the range of mantle viscosity models shown in Figure 2. The Ribe conversion is used to map finite strain into anisotropy on the assumption that perovskite behaves in a similar way to olivine. Viscosity model A, which produces natural strains of 7, generates 6–10 secs of shear-wave splitting. In contrast, the uniform viscosity mantle model (model B), with a predicted natural strain of 2, produces only 0–5 secs

of shear-wave splitting. Three other mantle viscosity profiles (models C, D and E), which incorporate viscosity increases at 410 km and 660 km depths, produce shear-wave splitting magnitudes 0.5–7.5 secs, 6 secs and 4.5–6 secs. Viscosity profiles with increases at 660 km depth generally produce more shear-wave splitting (3–8 secs at large epicentral distances and 0.5–3 secs at small epicentral distances) than models without this increase. This observation is explained by the larger finite deformation fields generated when a viscosity increase is present at 660 km depth. Viscosity models D and E have abrupt jumps in viscosity at 660 km depth, producing tt-residual trends that show consistent shear-wave splitting with epicentral distance. However, viscosity model A has a gradual viscosity increase at 660 km depth, and generates much more shear-wave splitting and this decreases with increasing epicentral distance. Viscosity model A spreads deformation over a large lateral extent in the topmost lower mantle, while in model E the large viscosity jump compresses the region of high natural strain into a much smaller and thinner region. Thus, model A produces greater amounts of shear-wave splitting. Dynamic recrystallization and/or diffusion creep would destroy some of the preferred orientation and consequently our model over-predicts the magnitude of anisotropy.

[14] The dependency of predicted shear-wave splitting magnitude on the different conversion schemes for finite strain to anisotropy has been examined (not shown here). The Ribe conversion predicts more splitting than the linear conversion, because the Ribe conversion saturates at a lower finite strain and produces more anisotropy, while the exponential conversion saturates even faster and produces still larger amounts of shear-wave splitting (8–12 secs).

[15] Figures 3b and 3c show the effect on shear-wave splitting of inherited deformation from above the 660 and 410 km phase transitions. For viscosity model A, we see that the magnitude of shear-wave splitting reduces from 7–10 secs to 4–6 secs of splitting when deformation accumulated above 410 km is ignored, and that this further reduces to 2–3 secs when all the accumulated deformation above 660 km is zeroed. The predicted splitting for a model when deformation above 660 km is set to zero is surprising, considering this model only produces natural strains of 2, however this can be explained by the saturation of anisotropy at small finite strain for the Ribe conversion. A similar pattern of behaviour is observed for viscosity model B but shear-wave splitting magnitudes are much smaller. Viscosity model A produces comparable amounts of shear-wave splitting as that observed by *Wookey et al.* [2002], when deformation above 410 km is set to zero but not above 660 km. This suggests that minerals that undergo phase transformations do inherit deformation accumulated by the previous mineral phase, but how much is unclear.

5. Summary

[16] Models of subduction body force stresses predict large deviatoric stresses (~40 Mpa) in a broad region within the topmost lower mantle when the subducting slab encounters a viscosity increase at the 660 km discontinuity. Finite strain calculations show that strain ellipses align in a similar region as that of the large deviatoric stresses. Ray tracing through these finite strain models produces in excess of 4 secs of shear-wave splitting when a viscosity increase is present at the 660 km discontinuity. The amount of shear-wave splitting generated is sensitive to not only the mantle viscosity structure and the amount of deformation inherited when a mineral undergoes a phase transformation, but also the method of conversion from finite strain to anisotropy. We conclude that when a slab encounters a viscosity increase at the 660 km discontinuity, it impedes its movement, which in turn produces large stresses in the topmost lower mantle. These stresses induce mineral alignment, and produce a region of anisotropy. We suggest that it is this anisotropic region, at the top of the lower mantle that generates the shear-wave splitting observed by *Wookey et al.* [2002]. Slab penetration through the 660 km phase transition into the lower mantle will generate further stresses in the topmost lower mantle, however the calculation of these stresses is complex and beyond the scope of this study.

[17] **Acknowledgments.** We would like to thank James Wookey and 2 anonymous reviewers for their useful comments and discussion. Stuart Nippress was supported by a NERC PhD studentship.

References

Ben Ismail, W., and D. Mainprice (1998), An olivine fabric database: An overview of upper mantle fabrics and seismic anisotropy, *Tectonophysics*, *296*, 145–157.

Blackman, D. K., and J.-M. Kendall (2002), Seismic anisotropy in the upper mantle: 2. Predictions for current plate boundary flow models, *Geochem. Geophys. Geosyst.*, *3*, 8602, doi:10.1029/2001GC000247.

Crotwell, H. P., T. J. Owens, and J. Ritsema (1999), The TauP toolkit: Flexible seismic travel-time and ray path utilities, *Seismol. Res. Lett.*, *70*, 154–170.

Dziewonski, A. M., and D. L. Anderson (1981), Preliminary Reference Earth Model (PREM), *Phys. Earth Planet. Inter.*, *25*, 297–536.

Fischer, K. M., and D. A. Wiens (1996), The depth distribution of mantle anisotropy beneath the Tonga subduction zone, *Earth Planet. Sci. Lett.*, *142*, 253–260.

Fischer, K. M., E. M. Parmentier, A. R. Stine, and E. R. Wolf (2000), Modeling anisotropy and plate-driven flow in the Tonga subduction zone back arc, *J. Geophys. Res.*, *105*, 16,181–16,192.

Hall, C. E., K. M. Fischer, and E. M. Parmentier (2000), The influence of plate motions on three-dimensional back arc mantle flow and shear-wave splitting, *J. Geophys. Res.*, *105*, 28,009–28,033.

Karato, S. (1998), Seismic anisotropy in the deep mantle, boundary layers and the geometry of mantle convection, *Pure Appl. Geophys.*, *151*, 565–587.

Kaufmann, G., and K. Lambeck (2000), Mantle dynamics, postglacial rebound and the radial viscosity profile, *Phys. Earth Planet. Inter.*, *121*, 301–324.

King, S. (1995), Models of mantle viscosity, in *Mineral Physics and Crystallography: A Handbook of Physical Constants*, *AGU Ref. Shelf*, vol. 2, edited by T. J. Ahrens, pp. 227–236, AGU, Washington, D. C.

Kusznir, N. J. (2000), Subduction body force stresses and viscosity structure at the 410 km and 660 km phase transition, *EOS Trans. AGU*, *81*(48), 1081.

Mainprice, D., G. Barruol, and W. Ben Ismail (2000), The seismic anisotropy of the Earth's mantle: From single crystal to polycrystal, in *Earth's Deep Interior: Mineral Physics and Tomography From the Atomic to the Global Scale*, *Geophys. Monogr. Ser.*, vol. 117, edited by S. Karato et al., pp. 133–159, AGU, Washington, D. C.

Malvern, L. E. (1969), *Introduction to the Mechanics of a Continuous Media*, Prentice-Hall, Old Tappan, N. J.

McKenzie, D. (1979), Finite deformation during fluid flow, *Geophys. J.*, *58*, 689–715.

Ribe, N. M. (1992), On the relation between seismic anisotropy and finite strain, *J. Geophys. Res.*, *97*, 8737–8747.

Silver, P. G. (1996), Seismic anisotropy beneath the continents: Probing the depths of geology, *Annu. Rev. Earth Space Sci.*, *24*, 385–432.

Sleep, N. H. (1973), Teleseismic *P*-wave transmission through slabs, *Bull. Seismol. Soc. Am.*, *63*, 1349–1373.

Steinberger, B. (2000), Slabs in the lower mantle: Results of dynamic modelling compared with tomographic images and the geoid, *Phys. Earth Planet. Inter.*, *118*, 241–257.

Steinberger, B., and R. Holme (2002), An explanation for the shape of Earth's gravity spectrum based on viscous mantle flow models, *Geophys. Res. Lett.*, *29*(21), 2019, doi:10.1029/2002GL015476.

Thomsen, L. (1986), Weak elastic anisotropy, *Geophysics*, *51*, 1954–1966.
Trampert, J., and J. van Heijst (2002), Global azimuthal anisotropy in the transition zone, *Science*, *296*, 1297–1299.
Vinnik, L., S. Chevrot, and J.-P. Montagner (1998), Seismic evidence of flow at the base of the upper mantle, *Geophys. Res. Lett.*, *25*(11), 1995–1998.
Wenk, H.-R., K. Bennett, G. R. Canova, and A. Molinari (1991), Modelling plastic deformation of periodotite with the self-consistent theory, *J. Geophys. Res.*, *96*, 8337–8349.
Wookey, J., J.-M. Kendall, and G. Barruol (2002), Mid-mantle deformation inferred from seismic anisotropy, *Nature*, *415*, 777–780.

N. J. Kusznir and S. E. J. Nippress, Department of Earth and Ocean Sciences, University of Liverpool, 4 Bownlow Street, Liverpool, Merseyside L69 3GP, UK. (nippress@liverpool.ac.uk)
J.-M. Kendall, School of Earth Sciences, University of Leeds, Leeds, UK.